

# 3-D Imaging Using Millimeter-Wave 5G Signal Reflections

Junfeng Guan<sup>ID</sup>, *Graduate Student Member, IEEE*, Arun Paidimarri, *Member, IEEE*, Alberto Valdes-Garcia<sup>ID</sup>, *Senior Member, IEEE*, and Bodhisatwa Sadhu<sup>ID</sup>, *Senior Member, IEEE*

**Abstract**—Emerging 5G millimeter-wave (mm-wave) networks use electronic beamforming and beamsteering and support signal bandwidths on the order of hundreds of MHz. Given these characteristics, opportunities exist to develop 3-D sensing applications that leverage 5G mm-wave communications infrastructure. In this context, this work introduces a signal processing pipeline that can: 1) accurately extract the Time of Flight (ToF) of reflected orthogonal frequency division multiplexing (OFDM) communications signals and 2) enhance range resolution by coherently aggregating the reflection information from separate frequency bands. In combination with precise beamsteering, the proposed signal processing techniques enable high-resolution 3-D radar imaging *without affecting communications protocols*. An experimental system demonstrating this concept has been implemented and is described. This system consists of two software-defined phased array radios (SDPARs), one configured as a prototype 5G base station TX, and one as an auxiliary prototype 5G RX. Each SDPAR primarily consists of a Si-based 28-GHz, 64-element, phased array transceiver module and software-defined radio. Simulation and benchmark results show that our coherent bandwidth stitching enables accurate OFDM-based ranging with 15-cm resolution. Measurement results show 3-D radar images of indoor scenes with 2° angular and 15-cm ranging resolution, created by processing reflected 5G-like communication waveforms at 28 GHz. The produced 3-D radar images effectively depict the location of objects in the scene, and these locations are in close agreement with the ground truth.

**Index Terms**—Bistatic radar, 5G, frequency modulated continuous wave (FMCW), imaging systems, imaging, millimeter-wave (mm-wave), orthogonal frequency division multiplexing (OFDM) radar, OFDM, passive bistatic radar, phased array radar, phased array, radar subsystem, radar, radars and communications systems, simultaneous communications and radar, software radios, software-defined phased array radio (SDPAR), 3-D sensing.

## I. INTRODUCTION

EMERGING 5G networks use wide-bandwidth and directional wireless communication in the millimeter-wave (mm-wave) spectrum. Such a network blueprint not only enables high-speed data links but also has strong potential for supporting sensing applications. Hundreds of MHz of available

Manuscript received February 3, 2021; revised April 1, 2021; accepted April 5, 2021. Date of publication May 26, 2021; date of current version June 3, 2021. (Corresponding author: Bodhisatwa Sadhu.)

Junfeng Guan was with the IBM Thomas J. Watson Research Center, Yorktown Heights, NY 10598 USA. He is now with the Department of Electrical and Computer Engineering, University of Illinois Urbana-Champaign, Urbana, IL 61820 USA.

Arun Paidimarri, Alberto Valdes-Garcia, and Bodhisatwa Sadhu are with the IBM Thomas J. Watson Research Center, Yorktown Heights, NY 10598 USA (e-mail: [avaldes@us.ibm.com](mailto:avaldes@us.ibm.com); [sadhu@us.ibm.com](mailto:sadhu@us.ibm.com)).

This article has supplementary material provided by the authors and color versions of one or more figures available at <https://doi.org/10.1109/TMTT.2021.3077896>.

Digital Object Identifier 10.1109/TMTT.2021.3077896

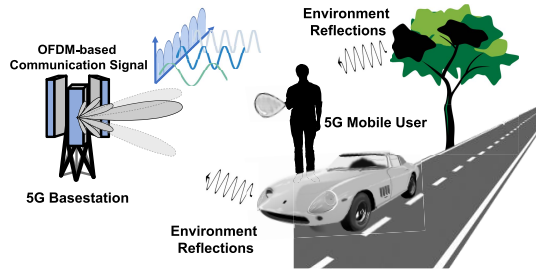


Fig. 1. Use case for 3-D imaging based on environmental reflections of 5G communications waveforms.

5G bandwidth can enable high range-resolution accuracy when employed for time-of-flight (ToF) measurement. In addition, fast beamsteering enables scene illumination and sensing in a specific set of directions. Given the expected widespread and dense deployment of mm-wave 5G technologies, introducing 3-D sensing capabilities to 5G base stations opens a plethora of urban-sensing application possibilities. For example, during every beam search scan, a 3-D radar image of the environment could be created, providing information such as traffic conditions, the presence of a scene anomaly (e.g., a fallen tree), or the presence of a drone. Ideally, such applications would be enabled without any modification to the hardware or the 5G communication waveform. A key challenge for implementing such an urban sensing vision is to enable 3-D radar functionality on top of 5G communication signals, at minimum cost, while not altering the communication functions or affecting the data throughput.

In this article, which is an expanded version of [1], we present an overlay sensing system prototype that utilizes reflected signals from directional 5G-like transmitted waveforms to extract 3-D radar information. An example use case is shown in Fig. 1, where a 5G base station is transmitting orthogonal frequency division multiplexing (OFDM) communication packets to mobile users by electronically steering directional beams. The transmitted communication signals are reflected by surrounding objects in the scene, such as cars, buildings, and trees. An auxiliary receiver extracts the ToF information for each reflection; using this information, the system can create a 3-D point-cloud image of the environment.

There have been several prior studies exploring joint radar and communication functions [2], [3]. A relatively straightforward approach involves the use of a communications device to transmit radar waveforms [4]–[6] and multiplex the communication and radar waveforms, using schemes such as time-division multiplexing [7], frequency-division multiplexing [8], space-division multiplexing [9]–[11], and code-division multiplexing [12], [13]. These approaches could

allow the reuse of part of the 5G communications infrastructure for imaging. However, it requires adding radar hardware and multiplexing radar and communications functions (in time/frequency/space/code), thereby increasing cost and reducing network data throughput. Moreover, such approaches would require the integration of new control functionality in the base station, which might not be amenable to modifications. An alternative is to design waveforms and code sequences that simultaneously perform communications and radar functions. Prior works in this area leverage chirped spread spectrum [14], [15], while others aim to design coding techniques that have favorable correlation properties for both radar and communication [16]–[19]. Additional prior works have attempted to embed information in frequency modulated continuous wave (FMCW) radar waveforms [20]–[24] or phase modulated continuous wave (PMCW) radar waveform [25]. Unfortunately, such waveforms entail tradeoffs between radar performance and communication data throughput; consequently, they would not satisfy 5G protocols.

The direct application of communication signals for radar functions has also been previously explored, with published results indicating that OFDM waveforms are a promising candidate [26]–[28]. Joint automotive radar and vehicular communication using OFDM-based IEEE 802.11ad waveform has also been studied [29]–[31]. However, these prior studies do not address the practical challenges of an actual hardware implementation (e.g., LO phase offsets and packet detection delay) and suffer from low range resolution due to limited channel bandwidth. Moreover, these prior publications either present simulation-only results [26], [28] or narrow bandwidth (93.1 MHz) and low-resolution (1.61 m) 1-D OFDM-based ranging results using bulky benchtop components [27]. Passive bistatic radar architectures that leverage an OFDM communications transmitter have also been widely studied [32]–[34]. This approach, however, requires capturing the broadcasted communications signal on a direct path as a reference, which might not be available in mm-wave 5G networks using highly directional beams. In addition, these architectures are incapable of 3-D imaging through beamsteering.

The signal processing techniques and associated prototype systems described in this work overcome the abovementioned challenges. Frequency-band-stitching and phased array beamforming are used to obtain high-resolution 3-D images while allowing OFDM-based communications to continue unaltered. To enable this functionality, we use an auxiliary receiver (RX) to monitor the reflected communications waveforms and extract ranging information by computing the time delay between the transmitted and received communications signals. *Our approach only adds auxiliary RX hardware elements to the 5G base station; it does not require any modification or altered control of the transmitter (TX) within the base station or its waveforms.*

In this work, the radar processing of the OFDM reflected waveforms is based on the insight that OFDM waveforms present a frequency-domain dual of FMCW waveforms. By creating a digital-baseband frequency-domain dual of the RF time-domain processing of FMCW waveforms, as described in Section II, we create radar images from

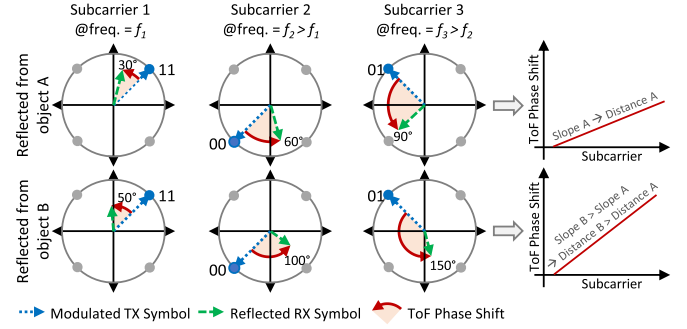


Fig. 2. OFDM-based ranging intuition: subcarrier phase shifts on the constellation plane and ranging using ToF phase shift slope information.

reflected OFDM waveforms. Moreover, once we synchronize the phase information of different packets transmitted at different times and in different frequency channels, we can combine this data to leverage a larger effective bandwidth and significantly improve the range resolution.

*Contributions:* The key contributions of this article are given as follows.

- 1) We present an FFT-based ranging algorithm based on a frequency-domain dual of FMCW radar and introduce solutions to implementation challenges.
- 2) We introduce an approach to stitching ranging data from multiple frequency channels to improve range resolution by increasing the sensing bandwidth. Stitching multiple channels allows the use of a complete GHz-wide 5G band enabling cm-range resolution.
- 3) Using the abovementioned techniques and a state-of-the-art 28-GHz software-defined phased array radio (SDPAR), we demonstrate, for the first time, a prototype system for 3-D-radar overlay sensing suitable for 5G communications infrastructure and waveforms.

The proposed system is evaluated first through simulation, where the super-resolved range profile is compared against baselines that directly apply the OFDM ranging theory. Then, the ranging accuracy and resolution of our system are further validated with ToF estimation benchmarks. Finally, imaging results from six indoor scenes are measured and compared against ground-truth 3-D point clouds captured by depth sensors. These results, as presented in detail in Section VI, validate the performance.

## II. THEORY OF RANGING USING OFDM WAVEFORMS

In this section, we present a detailed theoretical analysis and an intuitive explanation for ranging using OFDM communication signals. We also discuss a time–frequency duality between FMCW radar and OFDM ranging and leverage it in the development of an implementation pipeline for OFDM-based radar processing.

### A. OFDM-Based Ranging Intuition

An OFDM signal comprises multiple orthogonal subcarriers in frequency, which are modulated with parallel data streams. As the signal propagates in the air, each subcarrier experiences a phase shift, which is proportional to the ToF and the subcarrier frequency. As an example, let us consider

two scenarios corresponding to two objects, A and B, where object B is farther from the base station than object A. As shown in Fig. 2, ToF phase shifts proportional to frequency are introduced for the different subcarriers in each scenario. Moreover, the slope of the ToF phase shift versus subcarriers is directly proportional to the distance to the reflecting object. If we are able to extract the ToF phase shift slope versus the subcarrier in each beam direction, we can estimate the distance to the nearest reflector in that direction. Moreover, we can use superposition to resolve multiple reflectors in a given direction, as explained in Section II-D.

### B. OFDM-Based Ranging Detailed Theory

For OFDM transmission, the frequency-domain symbols encoded on the subcarriers are transformed to the time domain using inverse fast Fourier transform (IFFT). Hence, the time-domain baseband OFDM signal with  $K$  subcarriers and a subcarrier spacing of  $\Delta f$  can be written as

$$m(t) = \sum_{k=1}^K A_k e^{j(2\pi k \Delta f t + \psi_k)} \quad (1)$$

where  $A_k$  and  $\psi_k$  are the amplitude and phase of the symbol on the  $k$ th subcarrier. We upconvert this baseband OFDM packet to the passband frequency  $f_c$  for transmission:  $s(t) = m(t)e^{j2\pi f_c t}$ .

As explained earlier, in the proposed imaging system, a transmitter sends OFDM encoded communication data packets to receivers. The OFDM signal is also reflected by non-communicating physical objects in the environment. We use an imaging RX collocated with the TX to capture the reflected signals. Assuming a reflector at distance  $R$ , the received packet will be  $x_{\text{RX}}^{\text{BB}}(t) = \alpha_l s(t - \tau_l)$ , where  $\tau_l = (2R/c)$  is the round-trip ToF and  $\alpha_l$  is the attenuation in the reflection channel, including the reflectivity of the reflector. Recall the following property of the Fourier transform: a time shift causes a phase shift in the frequency domain. A time delay in the propagation introduces a phase shift in the subcarriers, which linearly increases with the *subcarrier frequency*, as seen from the frequency-domain representation of the RX baseband signal

$$X_{\text{RX}}^{\text{BB}}[k] = \underbrace{A_k e^{j\psi_k}}_{\text{TX modulation}} \cdot \underbrace{\alpha_l}_{\text{Gain}} \cdot \underbrace{e^{-j2\pi \Delta f \tau_l k}}_{\text{ToF phase slope}} \cdot \underbrace{e^{-j2\pi f_c \tau_l}}_{\text{ToF phase offset}}. \quad (2)$$

If we extract the phase shifts along with subcarriers and measure the resulting slope, we can estimate the ToF  $\tau_l$  and, hence, the distance of the reflector from the base station. To do so, we need to remove the symbol modulation on the subcarriers through an elementwise division between the reflected and transmitted symbols on each subcarrier, as shown in simulation in [26]. We draw a parallel between this OFDM-based overlay imaging technique and FMCW radar processing, as shown in Fig. 3 and explained in Section II-C.

### C. Time–Frequency Duality With FMCW Radar Waveform

Similar to the multicarrier OFDM waveform, the FMCW radar waveform also spans a wide range of frequencies. However, since it only has a single carrier, it sweeps the carrier frequency over time:  $x(t) = e^{j2\pi(\beta/2)t^2}$ , as shown in Fig. 3(f),

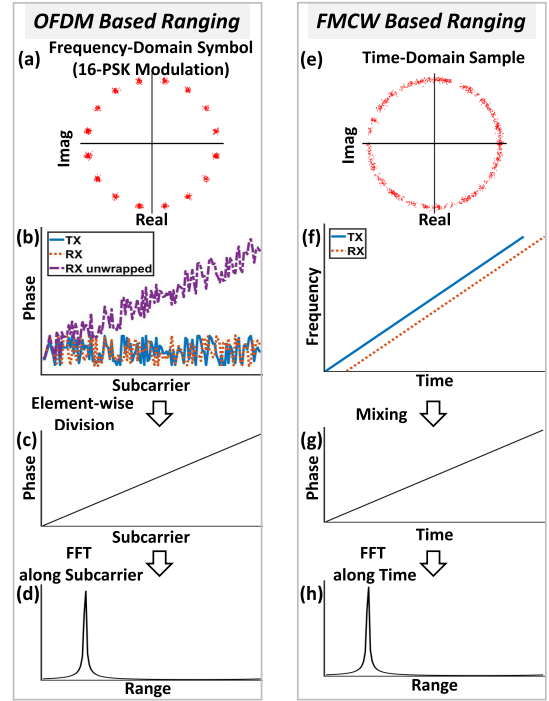


Fig. 3. (a) OFDM symbol constellation plane. (b) TX and RX OFDM subcarrier phases. (c) OFDM subcarrier phase shifts due to ToF. (d) OFDM range profile. (e) FMCW samples on the complex plane. (f) TX and RX FMCW carrier frequencies over time. (g) FMCW carrier phase shift over time due to ToF. (h) FMCW range profile.

where  $\beta$  is the slope of the FMCW frequency ramp versus time. The propagation delay also leads to a phase shift that linearly increases with the carrier frequency and, hence, with time

$$x(t - \tau_l) = \underbrace{e^{j2\pi \frac{\beta}{2} t^2}}_{\text{TX modulation}} \cdot \underbrace{\alpha_l}_{\text{Gain}} \cdot \underbrace{e^{-j2\pi \beta \tau_l t}}_{\text{ToF phase slope}} \cdot \underbrace{e^{j2\pi \frac{\beta}{2} \tau_l^2}}_{\text{ToF phase offset}}. \quad (3)$$

In order to extract the phase of the third term that is proportional to the ToF ( $\tau_l$ ), FMCW radar processing mixes the RX chirp with the TX chirp as a reference signal. Through this mixing operation, the TX chirp modulation is filtered and removed. As a result, the beat frequency signal has a phase shift along the time axis with a slope proportional to the ToF. This property is shown in Fig. 3(g)

$$x_{\text{fmcw-mixed}}(t) = \underbrace{\alpha_l}_{\text{Gain}} \cdot \underbrace{e^{-j2\pi \beta \tau_l t}}_{\text{ToF phase slope}} \cdot \underbrace{e^{j2\pi \frac{\beta}{2} \tau_l^2}}_{\text{ToF phase offset}}. \quad (4)$$

The OFDM frequency symbol on the subcarriers can be seen as a frequency dual to the time-domain FMCW signal. If we restrict the OFDM frequency symbols to have a unit amplitude (e.g., PSK), the OFDM constellation plane will have a similar pattern as the complex plane of FMCW samples, as shown in Fig. 3(a) and (e). Exploring this frequency–time duality between (2) and (3), we propose to process the OFDM waveform in the frequency domain similar to the way that FMCW signals are processed in the time domain, thereby extracting the ToF from the slope of the phase shift.

Considering the duality between the OFDM-based system and FMCW radar, we introduce a reference signal in the OFDM system corresponding to that used in an FMCW system and use a division operation in the frequency domain to

remove the TX modulation ( $A_k e^{j\psi_k}$ ), as shown in Fig. 3(b)

$$\begin{aligned} H[k] &= \frac{X_{\text{RX}}^{\text{BB}}[k]}{M[k]} = \frac{A_k e^{j\psi_k} \alpha_l e^{-j2\pi(k\Delta f)\tau_l}}{A_k e^{j\psi_k}} \\ &= \underbrace{\alpha_l}_{\text{Gain}} \underbrace{e^{-j2\pi(f_c+k\Delta f)\tau_l}}_{\text{ToF linear phase shift}}. \end{aligned} \quad (5)$$

This is shown in Fig. 3(c), where the slope versus frequency is now proportional to the ToF and free from TX modulation. From here, it is straightforward to adopt FMCW radar processing based on an FFT to extract the range profile. In the OFDM case, we perform an FFT on the channel frequency response  $H[k]$ , as shown in Fig. 3(d) [akin to performing an FFT on the time-domain signal in FMCW, as shown in Fig. 3(h)]

$$\rho[u] = F\{H[k]\} = \alpha_l \delta(u - \Delta f \tau_l) e^{-j2\pi f_c \tau_l}. \quad (6)$$

#### D. Extension to Multiple Reflectors & 3-D Imaging

The principles described above can be extended to the case of evaluating reflections from multiple objects. With reflections from  $L$  objects, and after dividing the baseband symbols elementwise by the reference symbols, we get  $H'[k] = \sum_{l=1}^L \alpha_l e^{-j2\pi(f_c+k\Delta f)\tau_l}$ , similar to the FMCW beat signal with multiple reflectors:  $\sum_{l=1}^L \alpha_l e^{j2\pi(-\beta l\tau + (\beta/2)\tau^2)}$ . The range profile can again be obtained using an FFT

$$\rho'[u] = F\{H'[k]\} = \sum_{l=1}^L \alpha_l \delta(u - \Delta f \tau_l) e^{-j2\pi f_c \tau_l}. \quad (7)$$

Moreover, with the beamforming capability of 5G base stations equipped with 2-D phased array antennas, we can further extend OFDM-based unidirectional ranging into 3-D imaging. For example, during the beam search/selection procedures, the base station TX sweeps its beam over different sectors while transmitting a reference signal (e.g., SSB or CSI-RS) [35]. The reflections from the beam search would allow us to image surrounding objects at different depths in each direction. Prior examples using mm-wave phased arrays for 3-D radar (using radar waveforms) are presented in [6] and [36].

### III. PRACTICAL CHALLENGES & SOLUTIONS

Simultaneously achieving radar-like ranging and high-throughput communication brings with it several implementation challenges. Unlike FMCW radar, where the chirp demodulation is done by mixing with the reference signal in the analog domain, the frequency-domain division in OFDM-based ranging requires digitizing the OFDM packet first. This requirement leads to three key challenges.

- 1) *Accuracy Under Phase Corruptions:* The digitized OFDM packet not only contains the channel parameters (i.e.,  $\alpha_l$  and  $\tau_l$ ) but also includes RX processing parameters [37]. These include the frequency/phase offsets caused by the mixing local oscillators (LOs) and analog-to-digital converter (ADC) sampling clocks in the RF signal downconversion and digitization. Moreover, in addition to the propagation delay, the digitized OFDM packet also experiences a random packet detection delay, which is typically orders of magnitude larger than the

ToF [38], [39], and can drown out the wanted ToF information. Therefore, to accurately estimate the ToF, we have to deembed the packet detection delay and other processing parameters from the channel parameters.

- 2) *Packet Detection on Reflection Channel:* OFDM packet detection algorithms leverage the autocorrelation characteristics of the repetitive preambles in the OFDM packets. However, these algorithms suffer in a 3-D imaging scenario, where the shortest line-of-sight (LoS) channel with high signal power is not available. Instead, the received OFDM packet consists of signals from multiple reflection paths with low SNR; as a result, the autocorrelation result has a lower primary peak but more secondary peaks. Therefore, a system that relies on packet detection on the reflection path would have a limited range.
- 3) *Resolution Limited by Signal Bandwidth:* The resolution of OFDM-based ranging is determined by the size of each FFT bin when we apply FFT across frequency  $f_{\min} = 1/K$ . Note that the ranging resolution, derived below, depends only on the OFDM signal bandwidth

$$\text{Resolution} = \frac{C \Delta \tau_{\min}}{2} = \frac{C f_{\min}}{2 \Delta f} = \frac{C}{2 K \Delta f} = \frac{C}{2B}. \quad (8)$$

Typical mm-wave 5G channels are limited to  $\sim 100$  MHz. This BW corresponds to  $\sim 1.5$ -m range resolution, about 10x worse than commercial FMCW radars [40], [41].

In the rest of this section, we present how we overcome these three challenges to achieve cm-level range resolution.

#### A. Practical System Model for OFDM-Based Ranging

To better understand the causes and effects of the practical challenges, we expand the theoretical model of OFDM-based ranging presented in Section II to incorporate the processing parameters in a practical system [37]. We also annotate the resulting unwanted phase shifts in the OFDM signal as it passes through the signal chain in Fig. 4.

The first processing parameter is the LO phase offset,  $\phi^{\text{TX}}$ , and gets added to the TX passband packet  $s'(t) = s(t)e^{j\phi^{\text{TX}}}$  at the upconversion mixer. Similarly, when we downconvert the reflected packets received by the auxiliary RX to baseband, an RX LO phase offset,  $\phi^{\text{RX}}$ , is introduced to the baseband signal. In addition, the carrier frequency offset (CFO),  $\delta f_c$ , between the base station TX and the auxiliary RX further corrupts the received signal

$$x'_{\text{RX}}^{\text{BB}}(t) = e^{j\phi_{\text{LO}}} e^{j2\pi\delta f_c t} \left[ \sum_{l=1}^L \alpha_l e^{-j2\pi f_c \tau_l} m(t - \tau_l) \right] \quad (9)$$

where  $\phi_{\text{LO}} = \phi_{\text{TX}} + \phi_{\text{RX}}$  represents the total LO phase offset.

Next, asynchronous baseband ADCs in the TX base station and auxiliary RX result in a sampling frequency offset (SFO) to the sampled  $x'_{\text{RX}}^{\text{BB}}(t)$ :  $n\delta T_s$ , where  $T_s$  is the sampling interval and  $n$  is the sample index. Furthermore, when we detect the OFDM packet and estimate the symbol timing, we end up with a packet detection delay, as annotated in Fig. 4. As a results, the digitized and

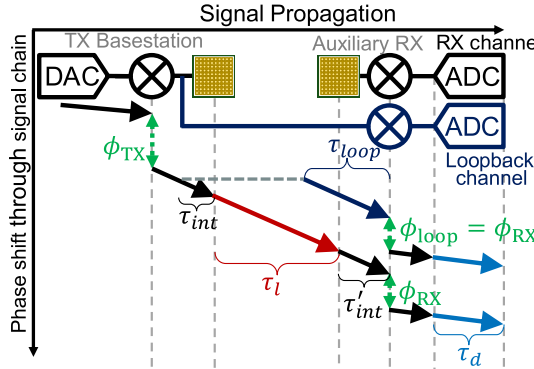


Fig. 4. Canceling unwanted phase shift through the signal chain using loopback channel at the RF frequency.

detected OFDM packet becomes:  $y[n] = x_{\text{RX}}^{\text{'BB}}[n - \tau_d + n\delta T_s]$ , and the corresponding frequency-domain symbol can be written as

$$Y[k]_{\text{RX}} = \underbrace{A_k e^{j\psi_k}}_{\text{TX modulation}} \underbrace{e^{j\phi_{\text{LO}}}}_{\text{LO phase offset}} \underbrace{e^{j2\pi\delta f_c n T_s}}_{\text{CFO}} \underbrace{e^{j2\pi k \Delta f n \delta T_s}}_{\text{SFO}} \\ \underbrace{e^{-j2\pi k \Delta f \tau_d}}_{\text{Packet Detection Delay}} \sum_{l=1}^L \alpha_l \underbrace{e^{-j2\pi(f_c + k \Delta f)\tau_l}}_{\text{ToF}}. \quad (10)$$

From (10), we observe that all four processing parameters either introduce a constant phase offset to all subcarriers (e.g., LO phase offset and CFO) or result in a linear phase shift proportional to the subcarrier frequency (e.g., packet detection delay and SFO). Although CFO and SFO can potentially be eliminated by synchronizing the base stations' TX and auxiliary RX LO and ADC, the LO phase offsets and packet detection delay remain in the OFDM symbols. Therefore, if we simply divide  $X[k]$  by the TX modulated symbols  $A_k e^{j\psi_k}$  on each subcarrier as per (5), the unknown parameters  $\Delta\phi_{b,k}$  and  $\tau_b^d$  still prevent the determination of unbiased estimators of  $\tau_l$ . In the following, for simplicity, we assume frequency and sampling synchronization between the TX base station and auxiliary RX to focus on resolving the LO phase offsets and packet detection. However, since CFO and SFO influence the OFDM symbols, in the same way, they can be eliminated using the same approach.

### B. Removing Packet Detection Delay Using Loopback

Compared to the constant phase offset on all subcarriers, the linear phase shift caused by the packet detection is more problematic to ToF estimation from a single OFDM packet. In order to remove this unknown delay, we introduce a loopback channel in our auxiliary RX. As shown in Fig. 4, we split the TX OFDM signal into two copies: the first is applied to the over-the-air channel and the second to a loopback channel through a fixed-length cable. Instead of measuring the absolute phase shifts in the over-the-air channel that incorporates all channel and processing parameters, we measure the phase difference between the auxiliary RX and loopback channels. We synchronize the two channels to equalize the processing parameters  $\phi_{\text{Loop}} = \phi_{\text{RX}}$  and  $\tau_d$ , as well as the CFO and SFO. Consequently, the common processing parameters cancel

out in the differential measurement, and the remaining phase difference provides an unbiased estimate of the desired ToF.

To this end, we design the loopback channel to be identical, well-matched, and time- and phase-synchronized to the RX channel. Moreover, we synchronously sample signals from the loopback and auxiliary RX channels and then align the FFT window for the two channels. The resulting demodulated OFDM symbols in the loopback channel can be written as

$$Y[k]_{\text{Loop}} = A_k e^{j\psi_k} e^{j\phi_{\text{LO}}} e^{-j2\pi k \Delta f \tau_d} e^{-j2\pi f_k \tau_{\text{Loop}}}. \quad (11)$$

When we divide reflection channel symbols by the loopback channel symbols on every subcarrier, we get

$$H[k] = \frac{Y[k]_{\text{RX}}}{Y[k]_{\text{Loop}}} = \sum_{l=1}^L \alpha_l e^{-j2\pi f_k (\tau_l + \tau_{\text{int}} + \tau'_{\text{int}} - \tau_{\text{loop}})}. \quad (12)$$

With the processing parameters canceled out along with the TX modulation, we obtain a clean linear phase shift along subcarriers corresponding to the ToF difference between the reflection and loopback channels. Finally, we compensate for the known propagation delay in the loopback channel  $\tau_{\text{loop}}$  and calibrate for the internal propagation delays unique to the RX channel  $\tau_{\text{int}}$  and  $\tau'_{\text{int}}$  to achieve accurate range estimation.

### C. Performing Packet Detection on Loopback Channel

We overcome the challenge of packet detection on the reflected waveform by instead performing packet detection on only the loopback signal. Since the loopback channel is a wired channel with very high SNR and no multipath effect, we can easily find the precise moment when the OFDM packet starts. More importantly, by doing so, there is no packet detection on the reflected channel, which allows us to image much larger distances since the poor SNR of weak reflected signals no longer limits the packet detection process.

Based on the packet detection results, we find the samples that correspond to the start and end of individual symbols and cyclic prefix (CP) for the loopback signal. We line up the FFT window for the auxiliary RX signal samples and the loopback signal samples after a CP-long set of samples from the start of the symbol as in standard OFDM demodulation. Although the packet in the RX channel arrives later than that in the loopback channel, as long as the extra delay is shorter than the CP, there will not be intersymbol interference in the FFT windows. That being said, it is desired for the loopback channel delay to be similar to the smallest RX channel ToF of interest.

### D. Improving Range Resolution Through Subband Stitching

As discussed above, by leveraging a loopback channel, we are able to accurately estimate the ToF in the reflection channel. However, as shown in (8), the range resolution is still limited by the bandwidth of the OFDM packet, which, for a given transmission, cannot exceed the 5G subband<sup>1</sup> bandwidth (e.g., 100 MHz). In order to improve the range resolution to centimeters, we try to stitch the subband channel frequency

<sup>1</sup>We use the term "subband" to refer to the 5G frequency channel to avoid confusion between the frequency channel and the reflection channel in our system model.

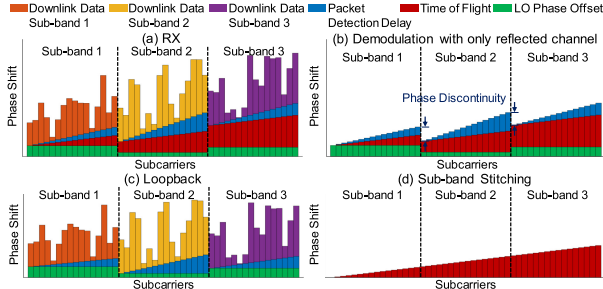


Fig. 5. Subband stitching by removing random time delays and phase offsets that vary from packet to packet. (a) RX. (b) Demodulation with only reflected channel. (c) Loopback. (d) Subband stitching.

responses ( $H$ ) to synthesize a wideband channel response that covers the generous overall 5G bandwidth available at 28 GHz, as shown in Fig. 5. Assuming that the reflectors remain static when packets in different subbands are sent, the reflection channel will be coherent for different packets.<sup>2</sup> We follow the bandwidth stitching guidelines developed for multiband radar [42] where the incoherence between subbands caused by the processing parameters is estimated and compensated for to make subband data mutually coherent. Then, standard ranging algorithms can be applied to the concatenated wideband data to obtain a superresolved range profile. Applying this guideline to our system requires all random linear phase shifts and constant phase offsets, as shown in Fig. 5(b), to be eliminated. This is because the random processing parameters vary from packet to packet and make the measured channel phase responses in multiple subbands incoherent.

However, in contrast to multiband radar where subband incoherence is processed in the digital domain, we leverage the analog loopback channel to equalize the delay and phase incoherence, as discussed in Section III-B. As can be seen from Fig. 5(a) and (c), our loopback signal shares the same processing parameters on all subbands with the RX reflected signal so that they can cancel out in the elementwise division. The resulting wideband channel frequency response only represents the ToF in the reflection channel and is coherent for all subbands. Note that the loopback channel response also needs to remain the same for all subbands. Besides, due to the orthogonality between 5G OFDMA subbands, there is no frequency incoherence between subbands allowing us to simply concatenate subband channel frequency responses in the frequency domain, as shown in Fig. 5(d). Finally, we apply FFT on the synthesized wideband channel frequency response as if from a single GHz-wide OFDM packet. A pseudocode for the super-resolution 3-D imaging algorithm is shown in Algorithm 1.

Note that stitching noncontiguous subbands is also possible, but the resulting spectral gaps lead to grating lobes in the output range profiles. These spectral gaps can be potentially filled through interpolation as in multiband radar [42].

<sup>2</sup>Channel estimation in a subband can be as short as a 5G NR slot (e.g., 1 ms), which is 10 ms for ten subbands, which is much faster than the typical speeds of everyday moving objects. Displacement of an object within a capture is nonideal since it will lead to motion blurring in the radar image.

---

### Algorithm 1 3-D Imaging With Bandwidth Stitching

---

```

for all TX BS beam direction  $\theta$  do
    Auxiliary RX PAAM steers to  $\theta$ 
    for b  $\leftarrow$  1 to B do
        Input: Synchronously sampled  $y_{\text{RX}}^b[n]$ ,  $y_{\text{Loop}}^b[n]$ 
        Packet detection on  $y_{\text{Loop}}^b[n]$ 
         $Y_{\text{Loop}}^b[k] \leftarrow \mathcal{F}\{y_{\text{Loop}}^b[n]\}$   $\triangleright$  FFT window aligned
         $Y_{\text{RX}}^b[k] \leftarrow \mathcal{F}\{y_{\text{RX}}^b[n]\}$   $\triangleright$  FFT window aligned
         $H^b[k] \leftarrow$  Subcarrier-wise division ( $Y_{\text{RX}}^b[k]$ ,  $Y_{\text{Loop}}^b[k]$ )
         $H \leftarrow$  Concatenate  $H^b$  for all b  $\triangleright$  Bandwidth Stitching
         $\rho_\theta \leftarrow \mathcal{F}\{H[k]\}$   $\triangleright$  FFT ranging
    Output: 3D spherical heatmap  $\leftarrow$  Aggregate  $\rho_\theta$  for all  $\theta$ 

```

---

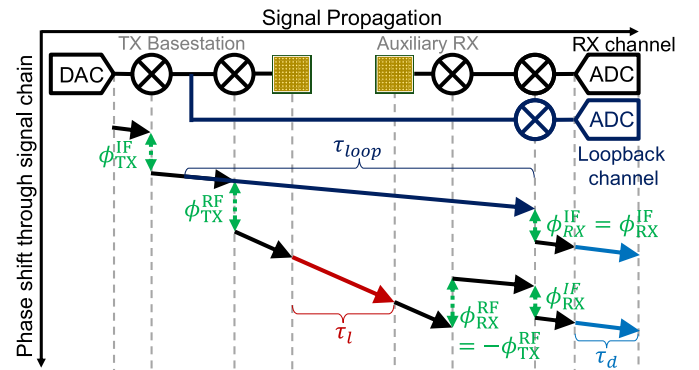


Fig. 6. Canceling unwanted phase shifts through the signal chain using loopback channel at the IF frequency.

### E. Loopback Channel Design Options

In Sections III-B–III-D, we assumed that the loopback channel is implemented at RF, and we showed that all phase corruptions from the processing parameters can be eliminated through the frequency-domain division by the loopback signal. Such loopback channel design would require an additional mm-wave front end and downconversion circuit, potentially raising the cost of the auxiliary RX. To address this concern, we can utilize an alternative loopback channel design at IF, which avoids the use of an additional mm-wave front end.

As shown in Fig. 6, we split the TX OFDM signal at the IF frequency and feed it to the loopback RX starting with the IF downconversion. Compared to the RF loopback channel, the IF loopback channel does not contain all the processing parameters in the RX channel. In particular, the loopback channel does not reflect the internal propagation delay in the mm-wave front end and the RF up/downconversion phase offsets that are unique to the RX channel. Therefore, these processing parameters have to be removed separately.

Since the internal propagation delay is fixed, it only needs to be calibrated once. On the other hand, the RF LO phase offset,  $\phi_{\text{LO}}^{\text{RF}} = \phi_{\text{TX}}^{\text{RF}} + \phi_{\text{RX}}^{\text{RF}}$ , is random and can lead to phase discontinuities at the channel boundaries, as we discussed in Section III-D. To overcome this challenge, we create a 180° phase difference between the RF up and downconversion LOs so that the opposite phase offsets cancel in the RX channel itself and do not appear in the RX OFDM subcarriers.

#### IV. OFDM-BASED RANGING PERFORMANCE ANALYSIS

In this section, we analyze the performance of the proposed OFDM-based ranging algorithm. First, we demonstrate that as an overlay system, our algorithm introduces no overhead to the underlying 5G communication. Then, we compare the ranging performance using OFDM to that obtained using FMCW waveforms based on standard radar metrics.

##### A. Compatibility With 5G Protocols

Our proposed 3-D ranging algorithm operates as an overlay to the underlying 5G communication functionalities. It does not require any modification to the TX data/constellation used to modulate the OFDM subcarriers, so it is able to reuse any OFDM-based communication packets sent by the TX base station including channel state information reference signals (CSI-RSs), and nonchannel estimation signals, such as synchronization signal and broadcast (SSB) blocks,<sup>3</sup> as well as data payload signals. This property is achieved because the subcarrier modulation is completely removed during the RX range processing. In fact, our overlay ranging approach is also TX data agnostic and preserves the privacy of user data since it does not decode or decrypt the TX data. Moreover, our algorithm also makes no assumptions regarding the SNR of the reflected RX waveforms since the packet detection performed on the loopback signal does not impose SNR requirements on the reflected signals. In order to obtain 3-D images of the environment, we can leverage the beam search/selection and user tracking procedures in 5G protocol, where the base station TX sweeps its beam over different directions while transmitting a reference signal (e.g., CSI-RS or SSB) [35].

However, relying only on reusing the 5G-NR communication protocols may restrict the field of view and resolution of the captured 3-D radar heatmap. This is because the highest sensing capability with the widest field of view and highest resolutions requires at least one downlink packet being transmitted to every direction and on every subband. When some subband packets are not available along with certain directions, the resulting range profile will have lower resolution and/or invisible angles. To obtain the highest possible sensing performance without affecting the communication traffic, our system can be combined with time-division-based joint sensing communication: during the downtime of OFDM communication traffic and when the resources are idle, we can opportunistically transmit short preamble-only sequences on all subbands and directions.

Finally, note that while we focus our attention on 5G communications in this article, our algorithm works for any multicarrier-based communications scheme and is not limited to 5G communications.

##### B. Subcarrier Modulation Scheme

For a constant average transmitted power level, our algorithm also does not depend on the OFDM subcarrier modulation scheme. Whether we use packets with a high-order

<sup>3</sup>These signals only occupy a limited number of subcarriers, which may lead to unknown frequencies in the channel frequency response ( $H[k]$ ).

TABLE I  
COMPARISON OF OFDM-BASED RANGING WITH FMCW RADAR

Metrics	FMCW Radar	OFDM-based Ranging
Duality	Time Sample (t)	Subcarrier (k)
Instantaneous frequency	$f_i = f_0 + \beta t$	$f_i = \Delta f k$
Amplitude	Unit for linear FMCW	Modulation dependent unit for PSK
Range resolution	$C/(2B)$	$C/(2B)$
Max unambiguous range	$T \frac{C}{2}$	$\frac{1}{\Delta f} \frac{C}{2}$
Max measuring range	$T \frac{C}{2}$	$\frac{1}{\Delta f} \frac{CP}{K} \frac{C}{2}$
Min measuring range	Reference signal	Loopback signal
SNR	$\alpha_l / \int n(t) dt$	$\alpha_l / \int N(f) df$

modulation (e.g., 256-QAM) or a low-order modulation (e.g., BPSK), our algorithm can achieve the same SNR in the output radar range profile. It can be proved that the SNR of the radar range profile shown in (6) is proportional to the reflection channel attenuation  $\alpha_l$  and the average SNR of the OFDM frequency symbols. Although, for high-order QAM modulations, different constellation points have different SNRs (outer constellation points have higher transmit power and, hence, higher SNR than the inner constellation points), the average symbol SNRs are the same for different modulation schemes. Therefore, for a given average transmit power, our algorithm is modulation scheme agnostic and is able to perform well with the high-order modulations with high data throughput, as defined in the 5G protocol. In practice, due to varying back-off requirements for different modulation schemes, the peak average power of higher order modulation schemes is typically lower than that of lower order schemes, resulting in a reduced communication range. This characteristic would then directly translate to a reduced imaging range as well.

##### C. OFDM-Based Radar Metrics

We next compare the ranging and imaging performance of OFDM-based ranging with that of FMCW radar by considering performance against common radar metrics, such as range resolution, maximum unambiguous range, maximal and minimal measuring range, and the signal-to-noise ratio of the resulting radar range profile. We summary the comparison results in Table I.

As we have shown in (8), the range resolutions of OFDM-based ranging and FMCW radar are both inversely proportional to the signal bandwidth:  $(C/2B)$ . Although the bandwidth of individual OFDM packets is limited by the subband bandwidth, our algorithm enables subband stitching to leverage the GHz-wide bandwidth of 5G mm-wave communication systems and, thus, achieves cm-level range resolution comparable to dedicated FMCW radars.

The maximum unambiguous range for OFDM-based ranging equals to the length of an OFDM symbol =  $(1/\Delta f)$  because the maximal phase shift in two adjacent bins

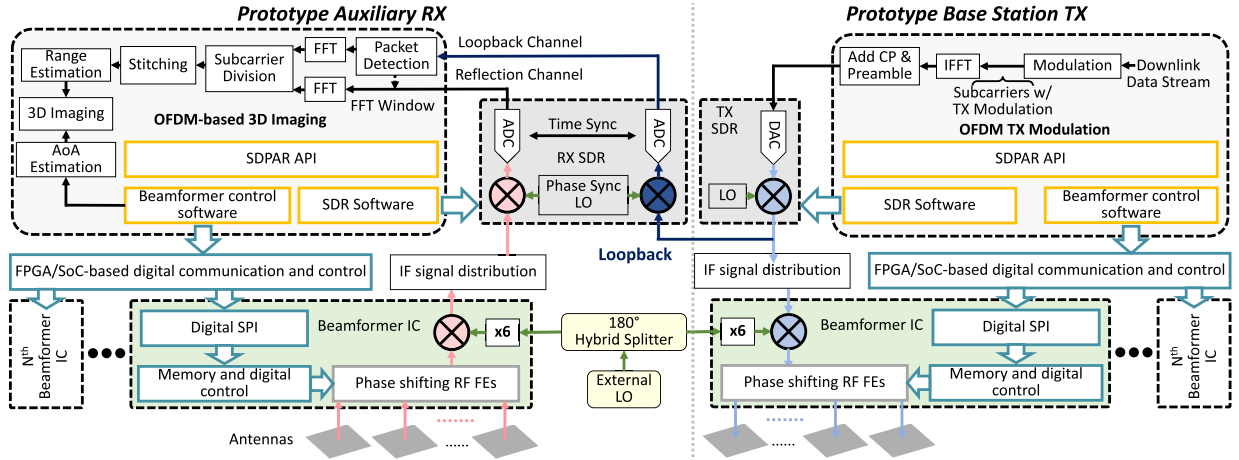


Fig. 7. Block diagram of the experimental hardware and software systems.

$2\pi \tau_{\max} \Delta f$  cannot exceed  $2\pi$ . This limit is again similar to the maximum unambiguous range for FMCW radar, which equals the length of the FMCW waveform  $T$  in this case. However, as we discussed in Section III-C, the maximal measuring range of our algorithm is further limited by the length of the OFDM CP. This limitation arises because (unlike the case of repetitive FMCW waveforms) adjacent OFDM symbols are modulated with different data and delays longer than the CP would cause intersymbol interference. Fortunately, a common CP of  $5 \mu\text{s}$  provides us with a maximal measuring range of 750 m, which is much larger than the 5G cell radius.

The SNR of the range profile obtained by OFDM-based ranging and that of FMCW radar are determined by the SNR of the frequency symbols and time-domain samples, respectively. FMCW radars have unit amplitude for all samples. If we assume that the OFDM symbols are also modulated with unit amplitude (e.g., PSK modulation) and are generated with the same transmit power and hardware noise figure, the SNR of FMCW time-domain samples and that of OFDM frequency symbols will be the same. Therefore, these approaches can achieve the same SNR in the radar range profile.

Our system focuses on fast-time processing (estimating the range of objects within a capture); however, slow-time processing can also be performed across symbols in a single OFDM packet, as described in [2].

## V. SYSTEM DESIGN—HARDWARE AND SOFTWARE

This section describes the implemented prototype system for 3-D imaging using 28-GHz OFDM communication signals. Fig. 7 shows a block diagram of our experimental setup comprising a prototype base station TX, an auxiliary imaging RX, and a signal processing pipeline implemented using Python in a PC. Although our prototype base station is capable of TRX operation, only the downlink (TX) mode is used since this is the only function relevant to our imaging experiments.

### A. Prototype Base Station TX

As shown in Fig. 7, the prototype base station hardware features an SDPAR similar to that described in [43]. The

28-GHz SDPAR features a Si-based 64-element dual-polarized TRX phased array antenna module (PAAM) comprising four 32-element phased-array ICs [44], [45] integrated in an organic antenna-in-package module [46]. The PAAM achieves performance similar to that of state-of-the-art mm-wave 5G base stations [47] and features 54-dBm saturated EIRP,  $\pm 60^\circ$  scan range in azimuth and elevation,  $1^\circ$  beamsteering resolution,  $12^\circ$  half-power-beamwidth,  $<10\text{-ns}$  beam switching time, and up to 20-dB sidelobe suppression. As a result, the SDPAR used in this work is representative of the hardware capabilities and performance expectations from current mm-wave 5G-NR base stations.

Compared to the USRP B200mini-based SDPAR used in [43] where the channel bandwidth was limited to  $<10$  MHz, the SDPAR in this work extends the baseband signal bandwidth to 100 MHz per channel (a typical bandwidth used for current 5G NR applications) using an Ettus USRP X310 baseband with UBX-160 daughter boards to implement the ADC/DAC and baseband  $\leftrightarrow$  IF frequency conversion functions. Channel switching is enabled by varying the LO frequency external to the PAAM.

TX packet generation follows a standard OFDM packet generation process with randomly generated data. Each OFDM packet comprises 8192 subcarriers (including 391 guard band subcarriers) with 12.2-kHz subcarrier spacing, similar to that in 5G NR. The waveform data are transmitted to the SDPAR USRP X310 over 10-Gb/s Ethernet where it is converted to analog and upconverted to 3 GHz to interface with the SDPAR PAAM. The USRP is controlled using the GNU Radio API [48]. The upconverted 3-GHz signal is split to create a loopback signal that is fed back to the auxiliary RX.

The PAAM used in the SDPAR features calibration-free beamforming, beamsteering, and beam tapering by leveraging loss-invariant phase shifters [49] and phase-invariant variable gain amplifiers (VGAs) [50] implemented on-chip. Fast beam control is enabled through index switching through rows of 128-row SRAM tables (one per phased array frontend). All beam controls are enabled from the same Python-based SDPAR API that is used for data transmission and reception. In our experiments, phased array tapering of 20 dB is used

to reduce spatial interference during communications and simultaneously serves to reduce radar sidelobe ambiguity. The beam configuration data in the TX are passed to the auxiliary RX to inform the image creation.

### B. Prototype Auxiliary RX

The prototype auxiliary RX hardware features the same SDPAR as the prototype base station. As shown in Fig. 7, the RX X310 USRP uses two inputs (the USRP features two RX channels): one from the RX SDPAR PAAM and the other as loopback from the prototype TX. As discussed in Section III, the loopback calibrates delays (and delay spreads) in USRP RX, ADC sampling, and OFDM packet detection. For our IF loopback implementation, a one-time calibration of static cable delay mismatch between the TX and RX SDPAR connections is performed.<sup>4</sup> The LOs of the TX and RX SDPARs are frequency synchronized using an external PLL, while their phase differs by  $180^\circ$ , achieved through the use of matched cables and a directional coupler. The auxiliary RX PAAM beam is set to mimic the beam configuration of the TX beam to provide additional spatial filtering and improve the spatial resolution of the image. Note that, in all radar systems, enough isolation between the TX and RX PAAM is needed. Higher power leakage than our prototype can be expected if the TX and RX PAAMs are packaged together. However, instead of mitigating crosstalk entirely in analog, we can adopt a hybrid scheme and utilize self-interference cancellation technologies [51] to subtract the leakage by our loopback signal in digital. In our experimental setup, we use an external 10-MHz clock as the common reference clock to the TX and RX PLLs and ADCs inside the USRPs. However, as we discussed in Section III-A, it is not required since the common CFO and SFO in the RX and loopback channels will cancel out in the elementwise division. Inside the auxiliary RX, the signal path and loopback path are phase synchronized as required (see Section II) using the GNU Radio API.

The digitized, 100-MHz-wide signal and loopback paths are received by the computer over a 10-Gb/s Ethernet connection. The OFDM ranging pipeline comprises cross correlation-based packet detection on the loopback channel, followed by CP removal, extraction of time-domain symbols, and FFT on the extracted symbols. Next, we perform the elementwise division of the frequency-domain RX symbols by the loopback symbols. The output wireless channel frequency responses are temporarily stored in memory until packets from the different 5G channels are processed. We then concatenate the subcarriers across channels in the frequency domain and use an FFT to extract the range profile. In our prototype system, we stitch 11 frequency channels of 96-MHz bandwidth each (after removing 4 MHz of guard band) to obtain a  $\sim$ 15-cm ranging resolution. Finally, we calibrate for the propagation delay in the loopback channel and align the range profile to the corresponding azimuth and elevation angle to get a 3-D range map in the spherical coordinate.

<sup>4</sup>Note that, while, in our system, we adopt an IF loopback channel to avoid an additional 28-GHz RF receive chain for the loopback channel, the loopback channel can also be implemented at RF using a physical connection or over-the-air leakage.

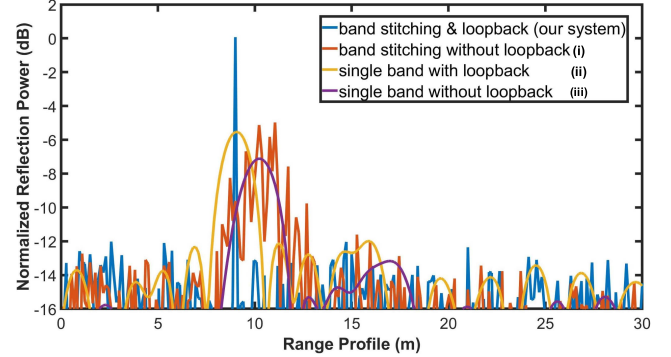


Fig. 8. Simulation of our signal in comparison with baselines without band stitching and loopback channel reference signals.

Note that, since our system does not modify the TX waveform or TX hardware in any way, there is no power penalty on the communications TX. The auxiliary RX, on the other hand, represents additional hardware and consumes power. However, the RX path computation required for 3-D imaging is expected to be significantly lower compared to the demodulation signal processing in a communications RX.

## VI. SIMULATION AND EXPERIMENTS

### A. Subsystem Simulation

First, we verify our bandwidth stitching and FFT-based ranging subsystems in simulation. Assuming a point reflector at 9 m, we simulate the reflected OFDM packets with random data modulation on eleven 100-MHz subbands along with the corresponding loopback signals. We also simulate the processing parameters in the RX and loopback packets to faithfully emulate the end-to-end system. We compare ranging accuracy and resolution of our method with three baselines: 1) single subband without loopback signal; 2) single subband with loopback signal; and 3) stitching all subbands without loopback signal. When the loopback signal is not available, we divide the RX subcarriers by the known modulated symbol as in [26] to remove the TX modulation. Fig. 8 demonstrates the range profiles obtained by the different methods. Range profiles estimated by baselines 1) and 2) have primary peaks beyond 9 m because the random packet detection is included in the estimated delay time. On the contrary, our method and baseline 2) are able to accurately predict a peak reflection power at 9 m by eliminating the packet detection delay using the loopback signal. Moreover, although 3) has access to the GHz-wide channel frequency response, its output range profile has many spurious peaks instead of a single primary peak. These spurious peaks are caused by the incoherent combination of multiple frequency subbands and are resolved in our method through coherent processing using the loopback signal. Therefore, the range profile generated by our method is not only accurate but also has a much higher resolution compared to baseline 2).

### B. Microbenchmark Measurements of Wired Channels

Here, we benchmark our subband coherence processing subsystem and evaluate the improved range resolution using

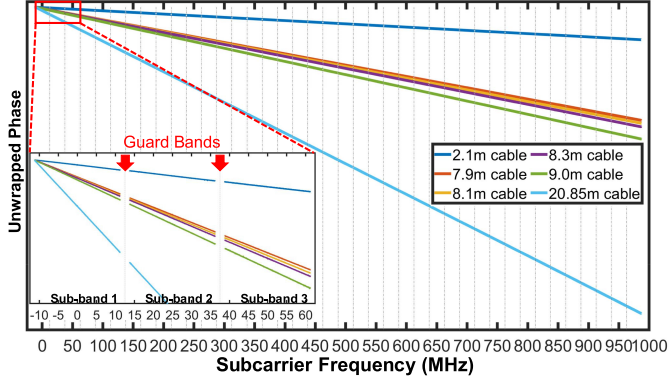


Fig. 9. Benchmarks of wire-channel ToF measurements: linear phase shift along subcarriers that is proportional to the ToF and remains coherent in multiple frequency subbands.

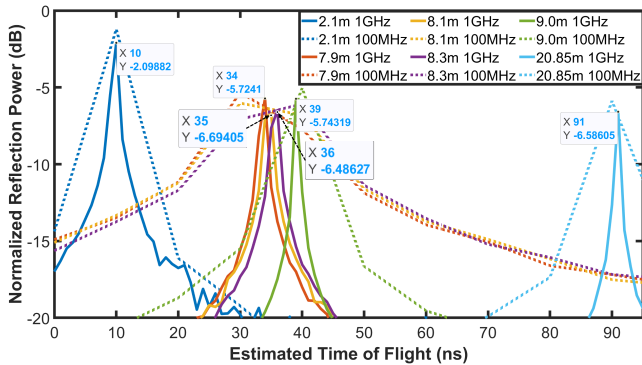


Fig. 10. Benchmarks of wire-channel ToF measurements: super-resolution and low-resolution ToF estimations obtained using FFT ranging on stitched 1-GHz and 100-MHz bandwidths.

bandwidth stitching. We replace the over-the-air RX channel with a wired channel with six coax cables with different lengths. In this experiment, we stitch 40 25-MHz subbands to synthesize a GHz-wide bandwidth and measure the channel phase response and ToF in the coax cables. From the channel phase response shown in Fig. 9, we can see the resulting linearly varying phase along with subcarriers, whose linearity in phase is proportional to the ToF and remains coherent across all subbands. This benchmark result demonstrates that our loopback signal can effectively cancel out the unwanted data modulations and RX processing parameters so that we can accurately estimate the propagation ToF and coherently process all subbands data. Fig. 10 shows the ToF estimation obtained by applying FFT on the mutually coherent GHz-wide channel frequency responses. We can see that  $\sim$ 1-ns ToF differences are distinguishable, which corresponds to  $\sim$ 21-cm coax cable length difference and  $\sim$ 15-cm ranging resolution in an over-the-air reflection channel.

### C. Wireless 3-D Imaging Experiments

Finally, we demonstrate the full-fledged imaging performance of our system using the prototype system shown in Fig. 11 to image seven indoor office locations. For each location, we steered the beam to 1426 directions within  $\pm 30^\circ$  in azimuth and elevation using 96-MHz OFDM data packets.

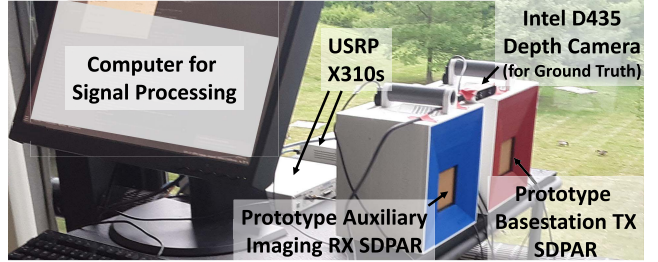


Fig. 11. Photograph of the experimental setup.

TABLE II  
COMPARISON OF DEPTH OF OBJECTS

Object	Our System	Ground Truth	Error
Scene i – monitor	157 cm	155 cm	2 cm
Scene i – chair	270 cm	266 cm	4 cm
Scene ii – monitor	256 cm	252 cm	4 cm
Scene iii – monitor	337 cm	342 cm	5 cm
Scene iv – pillar 1	222 cm	202 cm	20 cm
Scene iv – pillar 2	396 cm	383 cm	13 cm
Scene v – person	357 cm	361 cm	4 cm
Scene v – chair	265 cm	247 cm	18 cm
Scene vi – white-board	381 cm	372 cm	9 cm

TABLE III  
SUMMARY OF IMPLEMENTED SYSTEM CHARACTERISTICS

Phased array summary		Signal processing summary	
# elements	64	Channel bandwidth	100 MHz
# polarizations	2	# subcarriers	8192
Beam steering resolution	$1^\circ$	Subcarrier spacing	12.2 kHz
Beamwidth	$12^\circ$	# stitched channels	11
Beam scanning range	$\pm 60^\circ$	BW after stitching	1056 MHz
Saturated EIRP	54 dBm	Ranging resolution	$\sim$ 15 cm
		# voxels in 15m	$\sim$ 146,410

We repeated this beam sweep for 11 frequency channels to cover an overall bandwidth of 1056 MHz.

We demonstrate the 3-D images recreated by our system in Fig. 12 and compare them against the ground-truth RGB camera images and 3-D point clouds captured by an Intel D435 depth camera, as shown in Fig. 11. Note that the range of the D435 depth camera is limited to 3 m. For each scene, we show the 3-D radar heatmap captured by our system as a 3-D point cloud and a 2-D bird's eye view radar heatmap. The 3-D point clouds are generated by extracting the voxels whose reflected signal power surpasses a threshold, and its color code represents the reflected signal power. Similar to standard imaging radar heatmaps, the finite beamwidth of the phased-array front end acts as a sinc-function-shaped spread function on the reflectors along the angular axis. Thus, the resulting heatmap of the object is smeared around the highest power center at the same range. In addition, it is worth pointing out that the size of the objects in the 3-D radar images also depends on the radar cross section of the object with respect to the radios. Taking these intrinsic features of an imaging radar heatmap into consideration, the output of the 3-D images by our system

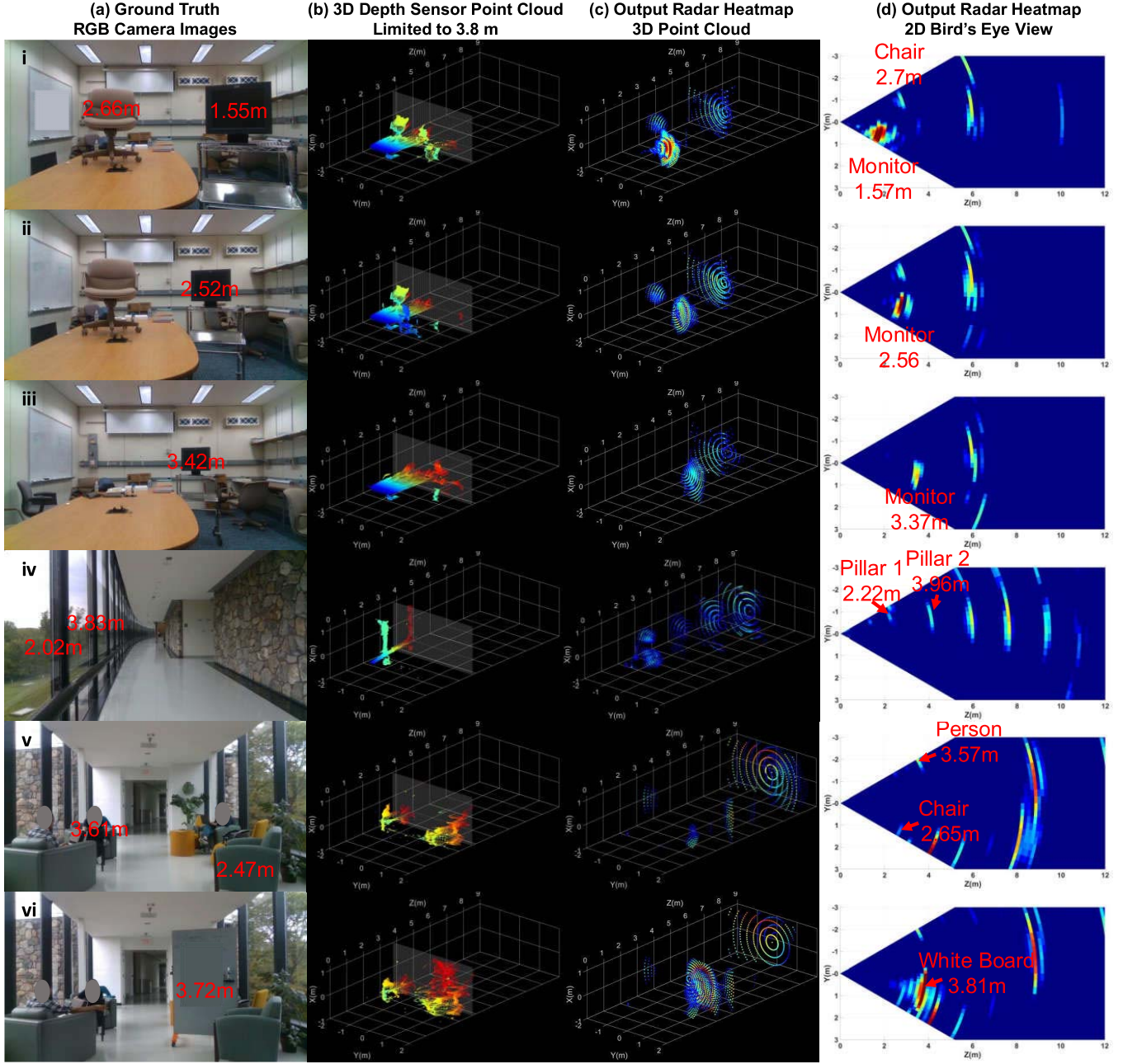


Fig. 12. Measured OFDM communications-based imaging showing (a) ground-truth RGB camera images, (b) ground-truth 3-D depth sensor point cloud (3-D depth sensor point cloud limited to 3.8 m), (c) reconstructed 3-D radar point clouds in column (output radar heatmap 3-D point cloud), and (d) 2-D bird's eye view of the 3-D output radar heatmap. We image several indoor settings: i: a conference room with a chair and monitor; ii: the same as i with the monitor moved back; iii: the same as ii with the monitor further back and chair removed; iv: office corridor with equispaced metal pillars; v: collaboration space with couches; and vi: the same as v with a whiteboard.

closely matches the scene. Moreover, we extract the depths for nine major objects in the seven scenes within the 3.5-m field of view of the depth sensor and evaluate the accuracy of the depth of the objects in Table II. The resulting median and mean depth errors are 5 and 8.7 cm, suggesting excellent agreement with the ground truth. These results demonstrate that our system is able to leverage the directional beamforming of a 5G phased array and use band stitching to achieve high-resolution 3-D imaging. The implemented system characteristics are summarized in Table III.

## VII. CONCLUSION

This article presented signal processing techniques and an associated system that can create a 3-D image of the physical environment surrounding an mm-wave directional communications device using reflected OFDM communication waveforms. The proposed signal processing pipeline is inspired by techniques used in FMCW radar and leverages mathematical similarities in the received signals between OFDM and FMCW when the OFDM signal is transformed into the frequency domain. The system solves practical technical challenges, such

as phase corruptions and packet detection delay uncertainties specific to OFDM systems, and stitches different subbands to create a high-resolution image. The system does not require any modification to the OFDM communication waveform, and its potential application to a 5G base station would only require the addition of auxiliary RX hardware components. This work is an example of the vast adjacent space application opportunities for directional mm-wave communication systems and the efficient exploration of such opportunities enabled by SDPARs.

#### ACKNOWLEDGMENT

The authors would like to thank Asaf Tzadok for technical discussions and the editors and anonymous reviewers for their feedback and comments.

#### REFERENCES

- [1] J. Guan, A. Paidimari, A. Valdes-Garcia, and B. Sadhu, "3D imaging using mmWave 5G signals," in *Proc. RFIC Symp.*, 2020, pp. 147–150.
- [2] C. Sturm and W. Wiesbeck, "Waveform design and signal processing aspects for fusion of wireless communications and radar sensing," *Proc. IEEE*, vol. 99, no. 7, pp. 1236–1259, Jul. 2011.
- [3] Z. Feng, Z. Fang, Z. Wei, X. Chen, Z. Quan, and D. Ji, "Joint radar and communication: A survey," *China Commun.*, vol. 17, no. 1, pp. 1–27, 2020.
- [4] F. Adib, Z. Kabelac, D. Katabi, and R. C. Miller, "3D tracking via body radio reflections," in *Proc. 11th USENIX Conf. Netw. Syst. Design Implement.*, Apr. 2014, pp. 317–329.
- [5] F. Adib, C.-Y. Hsu, H. Mao, D. Katabi, and F. Durand, "Capturing the human figure through a wall," *ACM Trans. Graph.*, vol. 34, no. 6, pp. 1–13, Nov. 2015.
- [6] A. Tzadok, A. Valdes-Garcia, P. Pepeljugoski, J. O. Plouchart, M. Yeck, and H. Liu, "AI-driven event recognition with a real-time 3D 60-GHz radar system," in *IEEE MTT-S Int. Microw. Symp. Dig.*, May 2020, pp. 795–798.
- [7] L. Han and K. Wu, "Joint wireless communication and radar sensing systems—state of the art and future prospects," *IET Microw. Antennas Propag.*, vol. 7, no. 11, pp. 876–885, Aug. 2013.
- [8] B. Ravenscroft, P. M. McCormick, S. D. Blunt, J. Jakabosky, and J. G. Metcalf, "Tandem-hopped OFDM communications in spectral gaps of FM noise radar," in *Proc. IEEE Radar Conf.*, May 2017, pp. 1262–1267.
- [9] A. Hassanien, M. G. Amin, Y. D. Zhang, and F. Ahmad, "Dual-function radar-communications: Information embedding using sidelobe control and waveform diversity," *IEEE Trans. Signal Process.*, vol. 64, no. 8, pp. 2168–2181, Dec. 2016.
- [10] P. M. McCormick, S. D. Blunt, and J. G. Metcalf, "Simultaneous radar and communications emissions from a common aperture, Part I: Theory," in *IEEE Radar Conf.*, May 2017, pp. 1685–1690.
- [11] P. M. McCormick, B. Ravenscroft, S. D. Blunt, A. J. Duly, and J. G. Metcalf, "Simultaneous radar and communication emissions from a common aperture, Part II: Experimentation," in *Proc. IEEE Radar Conf.*, May 2017, pp. 1697–1702.
- [12] X. Shaojian, C. Bing, and Z. Ping, "Radar-communication integration based on DSSS techniques," in *Proc. 8th Int. Conf. Signal Process.*, 2006, p. 4.
- [13] S. J. Xu, Y. Chen, and P. Zhang, "Integrated radar and communication based on DS-UWB," in *Proc. Int. Conf. Ultrawideband Ultrashort Impulse Signals*, 2006, pp. 142–144.
- [14] M. Robertson and E. R. Brown, "Integrated radar and communications based on chirped spread-spectrum techniques," in *IEEE MTT-S Int. Microw. Symp. Dig.*, vol. 1, Oct. 2003, pp. 611–614.
- [15] Y. Xie, R. Tao, and T. Wang, "Method of waveform design for radar and communication integrated system based on CSS," in *Proc. 1st Int. Conf. Instrum., Meas., Comput., Commun. Control*, Oct. 2011, pp. 737–739.
- [16] M. Jamil, H.-J. Zepernick, and M. I. Pettersson, "On integrated radar and communication systems using oppermann sequences," in *Proc. IEEE Mil. Commun. Conf.*, Nov. 2008, pp. 1–6.
- [17] X. Li, R. Yang, Z. Zhang, and W. Cheng, "Research of constructing method of complete complementary sequence in integrated radar and communication," in *Proc. IEEE 11th Int. Conf. Signal Process.*, Oct. 2012, pp. 1729–1732.
- [18] S. D. Howard, A. R. Calderbank, and W. Moran, "The finite heisenberg-weyl groups in radar and communications," *EURASIP J. Adv. Signal Process.*, vol. 2006, no. 1, p. 111, Jan. 2006.
- [19] A. Pezeshki, A. R. Calderbank, W. Moran, and S. D. Howard, "Doppler resilient golay complementary waveforms," *IEEE Trans. Inf. Theory*, vol. 54, no. 9, pp. 4254–4266, Sep. 2008.
- [20] X. Chen, X. Wang, S. Xu, and J. Zhang, "A novel radar waveform compatible with communication," in *Proc. Int. Conf. Comput. Problem-Solving*, 2011, pp. 177–181.
- [21] Z. Zhang, M. J. Nowak, M. Wicks, and Z. Wu, "Bio-inspired RF steganography via linear chirp radar signals," *IEEE Commun. Mag.*, vol. 54, no. 6, pp. 82–86, Jun. 2016.
- [22] M. Nowak, M. Wicks, Z. Zhang, and Z. Wu, "Co-designed radar-communication using linear frequency modulation waveform," *IEEE Aerosp. Electron. Syst. Mag.*, vol. 31, no. 10, pp. 28–35, Oct. 2016.
- [23] Z. Zhang, Y. Qu, Z. Wu, M. J. Nowak, J. Ellinger, and M. C. Wicks, "RF steganography via LFM chirp radar signals," *IEEE Trans. Aerosp. Electron. Syst.*, vol. 54, no. 3, pp. 1221–1236, Jun. 2018.
- [24] P. M. McCormick, C. Sahin, S. D. Blunt, and J. G. Metcalf, "FMCW implementation of phase-attached radar-communications (PARC)," in *Proc. IEEE Radar Conf.*, Oct. 2019, pp. 1–6.
- [25] S. H. Dokhanchi *et al.*, "Joint automotive radar-communications waveform design," in *IEEE Int. Symp. Pers., Indoor, Mobile Radio Commun. (PIMRC)*, 2017, pp. 1–7.
- [26] C. Sturm, T. Zwick, and W. Wiesbeck, "An OFDM system concept for joint radar and communications operations," in *Proc. IEEE Veh. Technol. Conf.*, May 2009, pp. 1–5.
- [27] C. Sturm, T. Zwick, W. Wiesbeck, and M. Braun, "Performance verification of symbol-based OFDM radar processing," in *Proc. IEEE Radar Conf.*, Jun. 2010, pp. 60–63.
- [28] Y. L. Sit, L. Reichardt, C. Sturm, and T. Zwick, "Extension of the OFDM joint radar-communication system for a multipath, multiuser scenario," in *Proc. IEEE RadarCon (RADAR)*, May 2011, pp. 718–723.
- [29] P. Kumari, D. H. N. Nguyen, and R. W. Heath, Jr., "Performance trade-off in an adaptive IEEE 802.11AD waveform design for a joint automotive radar and communication system," in *Proc. IEEE Int. Conf. Acoust., Speech Signal Process. (ICASSP)*, Mar. 2017, pp. 4281–4285.
- [30] R. C. Daniels, E. R. Yeh, and R. W. Heath, Jr., "Forward collision vehicular radar with IEEE 802.11: Feasibility demonstration through measurements," *IEEE Trans. Veh. Technol.*, vol. 67, no. 2, pp. 1404–1416, Feb. 2018.
- [31] P. Kumari, J. Choi, N. Gonzalez-Prelcic, and R. W. Heath, Jr., "IEEE 802.11ad-based radar: An approach to joint vehicular communication-radar system," *IEEE Trans. Veh. Technol.*, vol. 67, no. 4, pp. 3012–3027, Apr. 2018.
- [32] F. Colone, P. Falcone, C. Bongioanni, and P. Lombardo, "WiFi-based passive bistatic radar: Data processing schemes and experimental results," *IEEE Trans. Aerosp. Electron. Syst.*, vol. 48, no. 2, pp. 1061–1079, Mar. 2012.
- [33] J. R. Gutierrez Del Arroyo and J. A. Jackson, "WiMAX OFDM for passive SAR ground imaging," *IEEE Trans. Aerosp. Electron. Syst.*, vol. 49, no. 2, pp. 945–959, Apr. 2013.
- [34] C. R. Berger, B. Demissie, J. Heckenbach, P. Willett, and S. Zhou, "Signal processing for passive radar using OFDM waveforms," *IEEE J. Sel. Topics Signal Process.*, vol. 4, no. 1, pp. 226–238, Feb. 2010.
- [35] *Study on New Radio Access Technology Physical Layer Aspects*, document v14.2.0, 3GPB, Sep. 2017. [Online]. Available: <https://portal.3gpp.org/>
- [36] J. Plouchart, "Si-based 94-GHz phased array transmit and receive modules for real-time 3D radar imaging," in *IEEE MTT-S Int. Microw. Symp. Dig.*, Jun. 2019, pp. 532–535.
- [37] W. Dai, W. C. Lindsey, and M. Z. Win, "Accuracy of OFDM ranging systems in the presence of processing impairments," in *Proc. IEEE 17th Int. Conf. Ubiquitous Wireless Broadband (ICUWB)*, Sep. 2017, pp. 1–6.
- [38] D. Vasishth, S. Kumar, and D. Katabi, "Decimeter-level localization with a single WiFi access point," in *Proc. USENIX Symp. Netw. Syst. Design Implement. (NSDI)*, 2016, pp. 165–178.
- [39] H. Rahul, H. Hassanieh, and D. Katabi, "SourceSync: A distributed wireless architecture for exploiting sender diversity," in *Proc. ACM SIGCOMM Conf.*, 2010, pp. 171–182.
- [40] B. P. Ginsburg *et al.*, "A multimode 76-to-81GHz automotive radar transceiver with autonomous monitoring," in *IEEE Int. Solid-State Circuits Conf. (ISSCC) Dig. Tech. Papers*, Feb. 2018, pp. 158–160.

- [41] V. Giannini *et al.*, “9.2 A 192-virtual-receiver 77/79 GHz GMSK code-domain MIMO radar system-on-chip,” in *IEEE Int. Solid-State Circuits Conf. (ISSCC) Dig. Tech. Papers*, Feb. 2019, pp. 164–166.
- [42] K. M. Cuomo, J. E. Pion, and J. T. Mayhan, “Ultrawide-band coherent processing,” *IEEE Trans. Antennas Propag.*, vol. 47, no. 6, pp. 1094–1107, Jun. 1999.
- [43] B. Sadhu, A. Paidimarri, M. Ferriss, M. Yeck, X. Gu, and A. Valdes-Garcia, “A software-defined phased array radio with mmWave to software vertical stack integration for 5G experimentation,” in *IEEE MTT-S Int. Microw. Symp. Dig.*, Jun. 2018, pp. 1323–1326.
- [44] B. Sadhu *et al.*, “7.2 A 28 GHz 32-element phased-array transceiver IC with concurrent dual polarized beams and 1.4 degree beam-steering resolution for 5G communication,” in *IEEE Int. Solid-State Circuits Conf. (ISSCC) Dig. Tech. Papers*, Feb. 2017, pp. 128–129.
- [45] B. Sadhu *et al.*, “A 28-GHz 32-element TRX phased-array IC with concurrent dual-polarized operation and orthogonal phase and gain control for 5G communications,” *IEEE J. Solid-State Circuits*, vol. 52, no. 12, pp. 3373–3391, Dec. 2017.
- [46] X. Gu *et al.*, “Development, implementation, and characterization of a 64-element dual-polarized phased-array antenna module for 28-GHz high-speed data communications,” *IEEE Trans. Microw. Theory Techn.*, vol. 67, no. 7, pp. 2975–2984, Jul. 2019.
- [47] FCC. (Jan. 2018). *Ericsson AIR 5121 FCC Report*. Accessed: Mar. 31, 2021. [Online]. Available: <https://fccid.io/TA8AKRD901059-1/RF-Exposure-Info/RF-Exposure-information-3845517.pdf>
- [48] *GNU Radio*. Accessed: Mar. 31, 2021. [Online]. Available: <https://www.gnuradio.org>
- [49] Y. Tousi and A. Valdes-Garcia, “A Ka-band digitally-controlled phase shifter with sub-degree phase precision,” in *Proc. IEEE RFIC Symp.*, May 2016, pp. 356–359.
- [50] B. Sadhu, J. F. Bulzacchelli, and A. Valdes-Garcia, “A 28 GHz SiGe BiCMOS phase invariant VGA,” in *Proc. IEEE RFIC Symp.*, May 2016, pp. 150–153.
- [51] D. Bharadia, E. McMilin, and S. Katti, “Full duplex radios,” *ACM SIGCOMM Comput. Commun. Rev.*, vol. 43, no. 4, pp. 375–386, Sep. 2013.



**Alberto Valdes-Garcia** (Senior Member, IEEE) received the B.S. degree (Hons.) in electronic systems engineering from the Monterrey Institute of Technology, Toluca, Mexico, in 1999, and the Ph.D. degree in electrical engineering from Texas A&M University, College Station, TX, USA, in 2006.

In 2000, he joined Motorola Broadband Communications, Nogales, Mexico, as an RF Design Engineer. In 2006, he joined IBM Research, Yorktown Heights, NY, USA, where he is currently a Principal Research Staff Member and the Manager of the RF Circuits and Systems Group. Since 2009, he has been a Technical Advisory Board Member with Semiconductor Research Corporation, where he was the Chair of the Integrated Circuits and Systems Sciences Coordinating Committee in 2011 and 2012. In 2013, he was an Adjunct Assistant Professor with Columbia University, New York, NY. He has authored or coauthored more than 100 peer-reviewed publications. He is a co-editor of the book *60 GHz Technology for Gb/s WLAN and WPAN: From Theory to Practice* (Wiley, 2011). He holds more than 70 issued U.S. patents. His current research work is on millimeter-wave (mm-wave) systems for communications and imaging applications.

Dr. Valdes-Garcia has been serving as a member of the IEEE MTT-S Microwave and Millimeter-Wave Integrated Circuits Technical Committee since 2016, where he has been serving as the Chair since 2020. He is the Winner of the 2005 Best Doctoral Thesis Award presented by the IEEE Test Technology Technical Council. He was a recipient of the 2007 National Youth Award for Outstanding Academic Achievements, presented by the President of Mexico, and a co-recipient of the 2010 George Smith Award presented by the IEEE Electron Devices Society, the 2017 Lewis Winner Award for Outstanding Paper presented by the IEEE International Solid-State Circuits Conference (ISSCC), and the 2017 IEEE JOURNAL OF SOLID-STATE CIRCUITS (JSSC) Best Paper Award. Within IBM, he has been twice a co-recipient of the Pat Goldberg Memorial Award to the best paper in computer science, electrical engineering, and mathematics published by IBM Research in 2009 and 2017. He was inducted into the IBM Academy of Technology in 2015 and was recognized as an IBM Master Inventor in 2016 and 2019. In 2013, he was selected by the National Academy of Engineering for its Frontiers of Engineering Symposium. He has served on the IEEE 802.15.3c 60 GHz standardization Committee from 2006 to 2009. He also serves on the Inaugural Editorial Board of the IEEE JOURNAL OF MICROWAVES.



**Junfeng Guan** (Graduate Student Member, IEEE) received the B.S. degree in electrical engineering and the M.S. degree in electrical and computer engineering from the University of Illinois at Urbana-Champaign (UIUC), Urbana, IL, USA, in 2017 and 2019, respectively, where he is currently pursuing the Ph.D. degree at the Department of Electrical and Computer Engineering and the Systems & Networking Research Group.

His research interests are in the areas of wireless networking and sensing systems and mm-wave phased arrays.

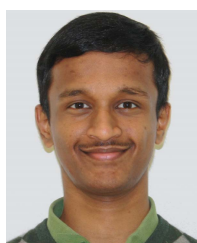
Mr. Guan was a recipient of the 2020 Qualcomm Innovation Fellowship. He received the Highest Honors at Graduation (B.S.) and the Edward C. Jordan Award from UIUC in 2017.



**Bodhisatwa Sadhu** (Senior Member, IEEE) received the B.E. degree in electrical and electronics engineering from the Birla Institute of Technology and Science, Pilani (BITS-Pilani), Pilani, India, in 2007, and the Ph.D. degree in electrical engineering from the University of Minnesota, Minneapolis, MN, USA, in 2012.

He is currently a Research Staff Member with the RF/mm-wave Communication Circuits & Systems Group, IBM Thomas J. Watson Research Center, Yorktown Heights, NY, USA, and an Adjunct Assistant Professor with Columbia University, New York, NY. At IBM, he has led the design and demonstration of the world's first reported silicon-based 5G phased array IC, a low-power 60-GHz CMOS transceiver IC for 802.11ad communications, a software-defined phased array radio, and a self-healing 25-GHz low-noise frequency synthesizer. He has authored or coauthored more than 50 peer-reviewed articles, the book *Cognitive Radio Receiver Front-Ends-RF/Analog Circuit Techniques* (Springer, 2014), and several book chapters. He holds more than 50 issued U.S. patents.

Dr. Sadhu serves as an IEEE MTT-S Distinguished Microwave Lecturer, the RFIC Systems & Applications Sub-Committee Chair, a Steering Committee Member of the IEEE RFIC Symposium, a TPC Member of the Wireless Subcommittee at IEEE International Solid-State Circuits Conference (ISSCC), and a Guest Editor of *IEEE TRANSACTIONS ON MICROWAVE THEORY AND TECHNIQUES* (TMTT). He has served as a Guest Editor for *IEEE JOURNAL OF SOLID-STATE CIRCUITS* (JSSC) in 2017. He was a recipient of the 2017 ISSCC Lewis Winner Award for Outstanding Paper (Best Paper Award), the 2017 IEEE JSSC Best Paper Award, the 2017 Pat Goldberg Memorial Award for the best paper in computer science, electrical engineering, and mathematics published by IBM Research, four IBM Outstanding Technical Achievement Awards, ten IBM Patent Plateau Awards, the University of Minnesota Graduate School Fellowship in 2007, the 3M Science and Technology Fellowship in 2009, the University of Minnesota Doctoral Dissertation Fellowship in 2011, the BITS Pilani Silver Medal in 2007, and stood second in India in the Indian School Certificate (ISC) Examination in 2003. He was recognized as an IBM Master Inventor in 2017 and was selected by the National Academy of Engineering for its Frontiers of Engineering Symposium in 2020.



**Arun Paidimarri** (Member, IEEE) received the B.Tech. degree in electrical engineering from IIT Bombay, Mumbai, India, in 2009, and the M.S. and Ph.D. degrees in electrical engineering and computer science from the Massachusetts Institute of Technology (MIT), Cambridge, MA, USA, in 2011 and 2015, respectively.

He is currently a Research Staff Member with the IBM Thomas J. Watson Research Center, Yorktown Heights, NY, USA. His research interests are in low-power wireless system design, mm-wave circuit design, and software-defined phased arrays.

Dr. Paidimarri is a member of the Technical Program Committees for the Radio Frequency Integrated Circuits (RFIC) Symposium and BiCMOS and Compound Semiconductor Integrated Circuits and Technology Symposium (BCICTS). He was a co-recipient of the Best Paper Awards at the IEEE International Conference on Communications (ICC) 2013 and SmartCom 2019. He was awarded the President of India Gold Medal in 2009. He won a Silver Medal at the 37th International Chemistry Olympiad held in Taipei, Taiwan, in 2005.